scientific reports

Check for updates

OPEN

Modeling the impact of intercellular signaling on dose metrics and therapeutic outcomes in spatially fractionated radiation therapy (SFRT) for lung cancer

Elnaz Balvasi[1], Farshid Mahmoudi[2]✉, Ghazale Geraily[1,3]✉, Parastoo Farnia[1,4] & Fatemeh Jafari[3]

Spatially fractionated radiation therapy (SFRT) delivers heterogeneous dose distributions to enhance tumor control while reducing normal tissue toxicity. Since conventional models like the linear-quadratic (LQ) model overlook intercellular signaling, a key factor in non-uniform fields, this study uses an advanced mathematical model to assess its impact on SFRT plan evaluation. A volumetric-modulated arc therapy (VMAT)-based SFRT framework was developed, resulting in two treatment plans: VMAT-GRID and 3D lattice radiation therapy (3D-LRT). A kinetic model incorporating both direct radiation damage and intercellular signaling was implemented to simulate signal dynamics, DNA damage, and calculate the survival ratio across 3D voxelized volumes. Key dosimetric and biological indices, including mean dose, equivalent uniform dose (EUD), valley-to-peak dose ratio (VPDR), therapeutic ratio (TR), and normal tissue complication probability (NTCP), were computed using both physical and biological doses. Incorporating intercellular signaling led to increased EUD, mean dose, VPDR, and NTCP, particularly in 3D-LRT plans with steeper dose gradients. Additionally, signaling effects caused extra biological damage in non-irradiated cells within low-dose regions, which resulted in a decreased TR. This study highlights that accounting for radiation-induced signaling alters the evaluation of SFRT plans compared to models considering only direct radiation effects. Therefore, to achieve accurate assessment, particularly in complex techniques like 3D-LRT, it is advisable to employ models capable of capturing both direct and indirect radiation responses. Additionally, experimental validation is a crucial step toward translating this model into clinical practice.

Keywords Spatially fractionated radiotherapy, GRID therapy, Volumetric-modulated arc therapy, Bystander effect, Intercellular signaling

Spatially fractionated radiation therapy (SFRT) is an innovative therapeutic approach that challenges the conventional paradigm of uniform dose delivery in radiotherapy and is particularly advantageous for treating large, unresectable, and radio-resistant tumors[1,2]. This approach employs highly modulated spatial dose distributions[3], achieved through techniques such as GRID therapy[4], Lattice Radiation Therapy (LRT)[5], Microbeam Radiation Therapy (MRT)[6], Minibeam Radiation Therapy (MBRT)[2] and FLASH Radiotherapy[7], to create alternating high-dose ("peaks") and low-dose ("valleys") regions within the tumor[3]. This is achieved through shielding tools such as blocks and multi-leaf collimators (MLCs), or advanced techniques like volumetric-modulated arc therapy (VMAT), which enable the formation of sharp dose gradients across the treatment field. As a result, unshielded tumor regions receive ablative doses (typically 15–20 Gy), while shielded areas are exposed primarily to scattered or sublethal radiation[2,8,9]. Despite this non-uniform dose distribution, clinical experience has shown surprisingly

[1]Department of Medical Physics and Biomedical Engineering, School of Medicine, Tehran University of Medical Sciences, Tehran, Iran. [2]School of Allied Medical Sciences, Lorestan University of Medical Sciences, Khorramabad, Iran. [3]Department of Radiation Oncology, Cancer Institute, Imam Khomeini Hospital Complex, Tehran University of Medical Sciences, Tehran, Iran. [4]Research Center for Intelligent Technologies in Medicine (RCITM), Advanced Medical Technologies and Equipment Institute (AMTEI), Tehran University of Medical Sciences (TUMS), Tehran, Iran. ✉email: farshidmahmoudi71@yahoo.com; gh-geraily@sina.tums.ac.ir; ghazalegraily@yahoo.com

uniform and effective tumor control along with enhanced normal tissue sparing. This paradox cannot be fully explained by classical radiobiological models that focus solely on direct DNA damage and the eradication of irradiated tumor cells[10]. Mounting evidence suggests that the biological efficacy of SFRT is not solely due to direct radiation effects but is also mediated by additional mechanisms, such as bystander effects, vascular alterations, stem cell migration and proliferation, abscopal responses, and immune system activation[2,3,11].

Among these, emerging data highlight the pivotal role of the bystander effect, particularly intercellular communication, in orchestrating the intercellular signaling responses within the heterogeneous dose distributions characteristic of SFRT. Bystander effects refer to biological responses that exceed what would normally be expected from the radiation dose received. These responses are generally triggered by the spread of reactive oxygen species (ROS) and the release of different cytokines[1–3,11–14]. This phenomenon challenges traditional metrics like physical dose distributions and dose-volume histograms (DVHs), which do not capture biological signaling dynamics[15,16]. While some researchers have used the linear-quadratic (LQ) model to calculate key parameters in SFRT, such as equivalent uniform dose (EUD) and therapeutic ratio (TR)[17–19], others have used bystander effect models to account for the impact of intercellular signaling on survival ratio[15,20–22]. Studies have shown that non-irradiated cells located in shielded regions of heterogeneous dose distributions (valleys) often exhibit lower survival rates than those predicted by the LQ model. This overestimation arises because the LQ model does not consider intercellular signaling from adjacent high-dose regions, which can induce additional damage in low-dose areas. Moreover, in high-dose regions (e.g., > 12 Gy), the LQ model loses predictive accuracy, as it was originally developed for lower dose ranges[7,15,23,24]. These limitations raise concerns about its reliability in the context of SFRT, highlighting the need for more robust approaches. In particular, they underscore the importance of developing biologically informed models that can simultaneously account for both direct radiation-induced effects and signaling-mediated responses in an integrated manner. Advancing such models will be pivotal for enhancing treatment planning accuracy and improving therapeutic outcomes in SFRT.

In this study, we employ an advanced mathematical modeling framework, based on the model proposed by McMahon et al.[20], that incorporates cell death due to both direct radiation damages and intercellular signaling effects, to evaluate VMAT-based SFRT plans for lung cancer.

Materials and methods

Patient selection and contouring

From the patient population at Imam Khomeini Hospital's Cancer Institute, a lung cancer patient with a GTV of 875.310 cm^3 was retrospectively selected. This study was conducted using anonymized CT scan images, with no personally identifiable information. Ethical approval was obtained from the Ethics Committee of Tehran University of Medical Sciences (Ethics code: IR.TUMS.IKHC.REC.1402.160). All methods were performed according to relevant guidelines and regulations. The Institutional Review Board (IRB) of Tehran University of Medical Sciences waived the requirement for informed consent. CT images of the patient were uploaded to the Elekta Monaco treatment planning system (TPS), version 5.10.02, where the GTV, relevant organs at risk (OARs), and main SFRT volumes were meticulously contoured under the guidance of an experienced radiation oncologist.

The virtual grid pattern consisted of three primary components: the GTV, unshielded areas (grid targets), and shielded areas (avoidance volume). This configuration enabled the creation of a high gradient dose distribution within the GTV volume, maximizing the delivered dose to the grid targets while minimizing radiation exposure to surrounding OARs (13).

This study designed two distinct virtual grid patterns for SFRT: the VMAT-GRID plan, characterized by parallel cylindrical targets, and the 3D-LRT plan, which employed spatially distributed spherical targets. In both plans, an internal margin was defined within the GTV to ensure that the edges of all targets remained at least 1 cm away from surrounding organs at risk (OARs).

For the VMAT-GRID plan, cylindrical targets with a diameter of 1 cm, using the 2D static brush tool, were created by first drawing circular cross-sections within the internal margin in 2D slices along the x–y plane. A center-to-center spacing of at least 6 cm was maintained to enhance dose sparing between adjacent targets. These circular contours were then interpolated across all axial slices, resulting in continuous cylindrical volumes aligned with the tumor's longitudinal (z) axis. This approach enabled the generation of uniform cylindrical grid targets while preserving both geometric conformity and the desired inter-target spacing within the GTV. For the 3D-LRT plan, spherical targets with a diameter of 1 cm were placed using the 3D static brush tool, also within the defined internal margin. A center-to-center distance of at least 3 cm in the sagittal and coronal planes and 6 cm in the axial plane was maintained to ensure spatial separation and minimize overlap of high-dose regions. In total, three cylindrical targets were placed for the VMAT-GRID plan and nine spherical targets for the 3D-LRT plan. The 3D spatial arrangement of these grid targets within the GTV is illustrated in Fig. 1.

Treatment planning

Using 6 MV flattening-filter-free (FFF) photon beams, single-fraction doses of 15 and 20 Gy were prescribed to the isocenter of the grid targets. Dose heterogeneity constraints were applied to optimize the treatment plans. Three full arcs were employed for cylindrical grid targets, while four partial arcs were used for spherical grid targets. This arc selection strategy was intended to optimize dose conformity to the grid structures while minimizing exposure to surrounding healthy tissues.

Intercellular signaling model

When predicting the response to radiation, most mathematical models primarily focus on the direct effects of radiation. However, to obtain a comprehensive understanding of the overall cellular response, indirect radiation

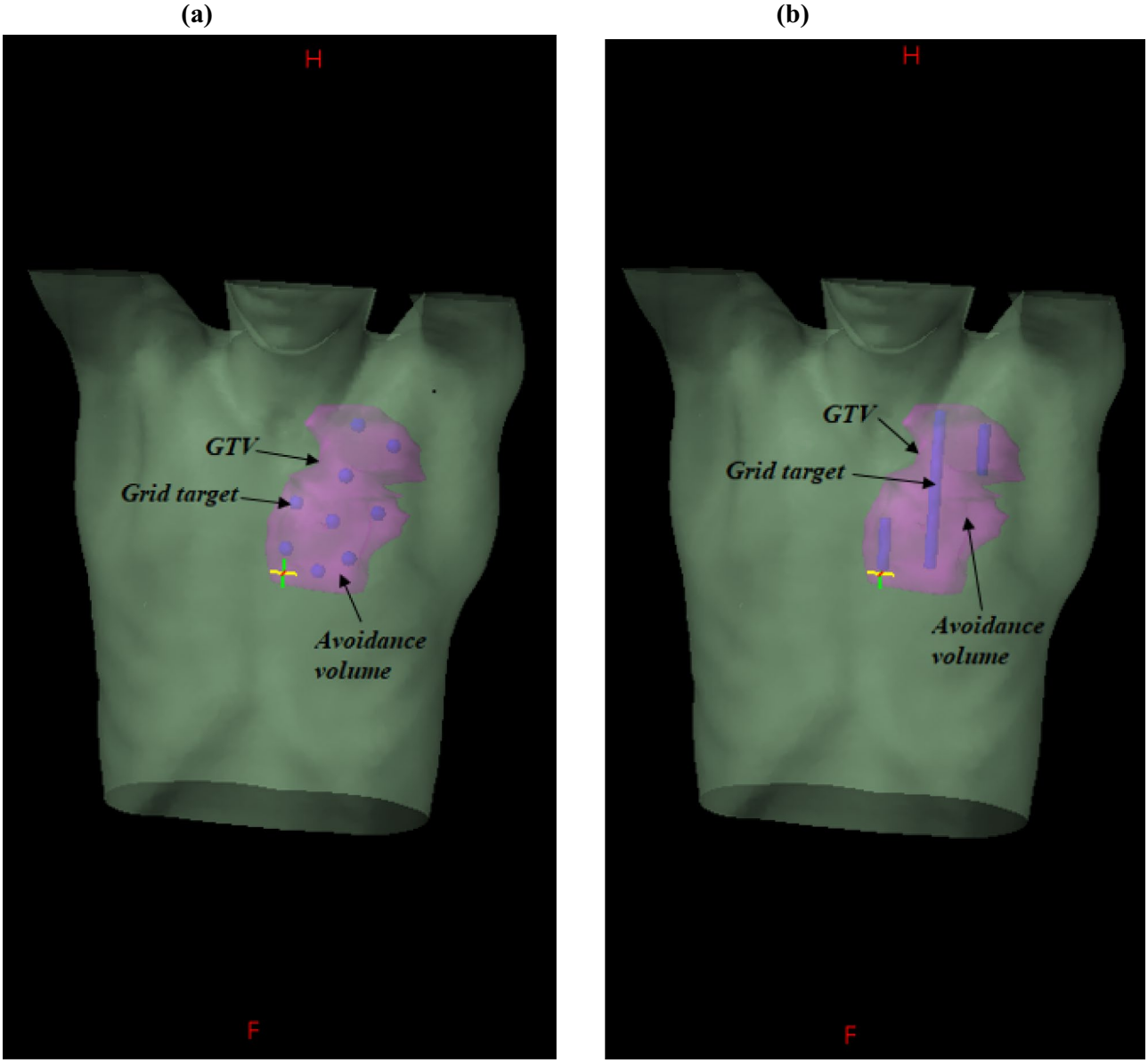

Fig. 1. Arrangement of grid targets within the GTV for 3D-LRT (**a**), and VMAT-GRID (**b**) plans.

effects must also be considered. Several models have been developed to simulate these indirect effects[21,24–32], but they are mostly suited for analyzing simple irradiation scenarios in laboratory settings. In this study, the model developed by McMahon et al.[20] was employed to account for both direct and indirect radiation effects in three-dimensional structures. This model provides a potentially improved approximation of signaling responses in heterogeneous dose distributions, which is particularly relevant for SFRT when compared to the conventional LQ model, which neglects non-targeted effects. The implementation of this model was carried out using MATLAB Software. MATLAB operates with discrete values rather than continuous variables; therefore, numerical analysis, particularly the finite difference method, was necessary to discretize the model's differential equations. In this model, the cell cycle, cell cycle arrest at various phases, and radiation-induced DNA damage arising from direct interactions with radiation and indirect effects mediated by radiation-induced signals were simulated to estimate the cell survival fraction following exposure to spatially heterogeneous virtual SFRT fields.

Although various biological mechanisms such as ROS, cytokines, and exosomal miRNAs have been implicated in bystander signaling, this study does not attempt to model each individually. Instead, following previous approaches, the bystander effect is represented as a single spatiotemporal signal concentration, ρ[15,20,33]. This study divided the simulation domain into discrete voxels, each assigned to a specific cell line. Cells located within each irradiated voxel experienced direct radiation-induced damage. Additionally, these cells began producing signals for some time (t_{sig}) proportional to the absorbed radiation dose (D). The duration of signal production is given by Eq. 1:

$$t_{sig} = \gamma D \quad (1)$$

In this equation, γ is a characteristic of the cell line. As the cells produce the signal, they aim to reach a maximum concentration in the environment. While actively signaling, cells aim to sustain a local concentration at ρ_{max}. This is modeled by a linear decrease in signal production as ρ increases, expressed as $\eta \frac{\rho_{max}-\rho}{\rho_{max}}$, where η is the signal production rate of a cell and a cell-line specific constant. Therefore, the signal production rate is initially at its highest when no signal is present in the environment. It gradually decreases over time as the signal level approaches the maximum concentration. The signals generated from radiation absorption are unstable and eliminated from the environment over time with a decay constant λ. The observation of these signals in various cell lines supports the assumption that the value of this constant is independent of the source cell type and remains unchanged[34]. Therefore, under uniformly continuous irradiation, the signal concentration initially increases due to the high production rate and approaches an equilibrium level. It then reaches a steady-state concentration, which is maintained for a duration of t_{sig}. After this period, signal production ceases, and only exponential decay continues, causing the signal concentration to decrease gradually over time. Figure 2 schematically illustrates the temporal variation of the signal concentration.

If the cell population is exposed to non-uniform irradiation, the concentration of the produced signal will vary across different regions of the field. As a result, these signaling molecules begin to migrate along the concentration gradient, leading to changes in signal distribution across the tissue. This redistribution alters the local signal concentrations and consequently modifies the level of biological damage compared to uniform irradiation. The produced signal can potentially elicit a response in a cell exposed to it. This response manifests as biological damage. Studies have shown that there are distinct thresholds for the generation of intercellular signals[23,32]. Once the signal concentration exceeds the defined threshold level ($\rho_{threshold}$ or ρ_t), the cell begins to respond, as these signals only elicit a reaction above this threshold[32]. The threshold concentration was determined by comparing simulation results with experimental data[20]. The extent of damage induced in a cell is proportional to the exposure duration (τ) during which the signal concentration exceeds the threshold level ($\rho > \rho_t$); this time interval is shown in Fig. 2.

The cellular response is binary: cells either respond to the signal and experience a specific level of damage, or they do not respond at all and remain unaffected. The probability of a cell responding to intercellular signals (PB) is defined by the following equation:

$$PB = 1 - e^{-\kappa\tau} \quad (2)$$

In this equation, κ is the response constant, which is specific to the cell line. Both the cells directly exposed to radiation and those that have not received any radiation can experience signal-induced damage.

Damage accumulation and survival

DNA damage, whether caused directly by radiation or indirectly through genotoxic stress initiated by intercellular signaling, is represented as a series of "hits", referring to potentially lethal events like complex or unrepaired double-strand breaks. Depending on the cell type, the specific phase of the cell cycle, and the number of hits received by the target, these hits could ultimately result in cell death. In this framework, after irradiation, the number of hits delivered to the cellular target was modeled as a function of the absorbed dose and the bystander

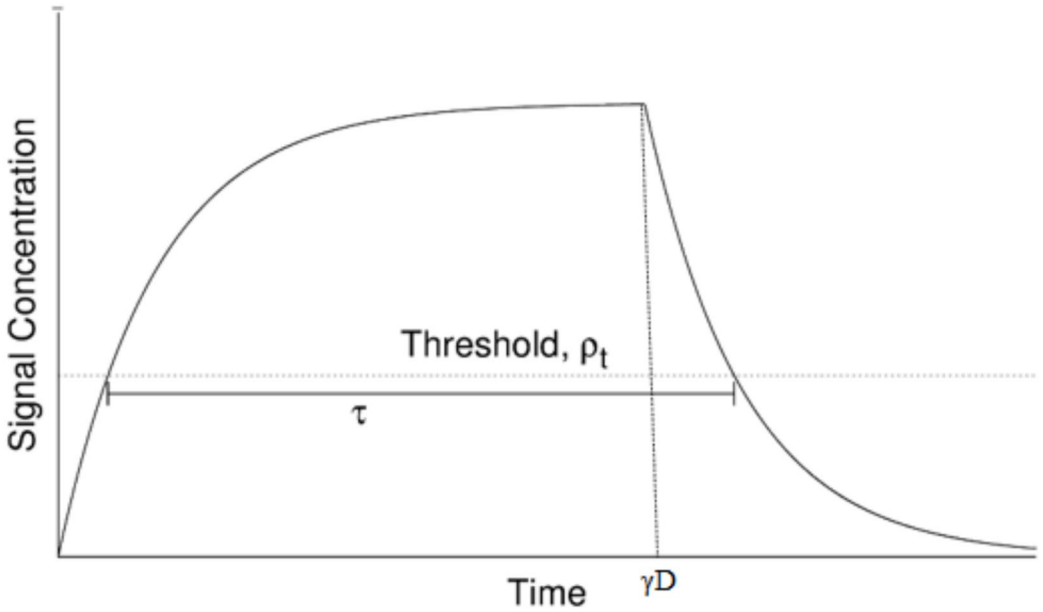

Fig. 2. Temporal variation of intercellular signal concentration[20].

signals received from neighboring irradiated cells. The number of hits caused by direct beam interactions is modeled using a Poisson distribution with a defined mean value equal to the product of the absorbed dose (D) and the number of hits per unit dose (HPG), i.e., HPG × D. HPG is a cell line-specific constant. In addition to this direct damage, the model accounts for the biological effects of intercellular signaling by introducing extra DNA double-strand breaks in certain cells, mimicking the impact of direct radiation. Additional damages, termed bystander hits (HB), follow a Poisson distribution, with a mean value specific to the cell line. This mean value, HB, represents the typical bystander response of the cell line and is determined by fitting the model to experimentally observed bystander response data[23,33,35]. Therefore, the model does not treat bystander damage as a sequential process following direct damage, but rather considers it a concurrent contributor to total cellular injury. This combined damage, comprising both direct and bystander-induced hits, is then used to evaluate the probability of cell survival or death, based on the cell's position in the cell cycle and the functionality of its checkpoint mechanisms. The cell fate depends on the extent of accumulated damage and the phase-specific sensitivity: cells receiving five or more hits to critical targets undergo immediate death, regardless of the cycle phase. In the G1 phase, three or more hits lead to cell cycle arrest, halting proliferation and eventually causing elimination. Conversely, cells in the G2 phase are more vulnerable, with even a single hit sufficient to trigger cell death. Importantly, the outcome is also modulated by checkpoint integrity; for example, in cells with defective p53, the G1 arrest was removed from the cell cycle progression, allowing damaged cells to bypass arrest and continue cycling despite unrepaired damage. However, in this study, both cell lines were assumed to express wild-type p53. Accordingly, an intact G1 checkpoint was included in the model, allowing all cells to undergo G1 arrest in response to DNA damage. This checkpoint behavior was implemented as a cell line–specific property and was uniformly applied across all cells of a given type. Additionally, damaged cells that remain viable and are not arrested continue to progress through the cell cycle and may incur 0 to 3 additional hits during DNA replication and mitosis. Finally, to account for the repair of sublethal damage in some cells, a further step is incorporated where, upon receiving a non-zero number of hits, one hit is subtracted from the total. This mechanism reduces the accumulation rate of cellular damage at low doses and leads to the formation of shoulder-shaped dose–response curves. Further details on the rationale and development of this model are available in earlier publications[15,20,33].

Three-dimensional signaling modeling

DICOM-RT objects (RT Image, RT Structure Set, and RT Dose) were extracted from the Monaco TPS and imported into a custom MATLAB program (version R2021a). The program segmented the desired volumes into 3D voxels with a volume of 1 mm^3. Each voxel is treated as a volume containing a uniformly irradiated cell population. The integration of the DNA damage model with the previously detailed bystander signaling framework allows for predicting the response of an individual cell within a population to a defined radiation field, incorporating the indirect effects of radiation. The dynamics of bystander signal production, diffusion, and decay were simulated concurrently beginning at $t = 0$, the onset of irradiation, with the initial intercellular signal concentration set to zero. The simulation was performed in discrete time steps of 1 s ($\Delta t = 1$ s). For each interval from t to $t + \Delta t$, the concentration of signals in each voxel was updated according to the following principles. Based on Eq. (3), each voxel received an increment in signal concentration relative to its value in the previous time step. This process continued until $t = t_{sig,}$ at which point the cells stopped producing signals, effectively removing the source of signal generation.

$$\rho\left(t+\Delta \mathrm{t}\right)=\eta\frac{\rho_{max}-\rho\left(t\right)}{\rho_{max}} \tag{3}$$

In this model, ρ(t) denotes the instantaneous signal concentration, while ρ_{max} represents the target maximum concentration that each voxel tends to approach. The difference between ρ_{max} and ρ(t) governs the amount of signal generated at each time step. At the onset of irradiation, when the signal concentration is zero, the production rate is highest. As the concentration nears ρ_{max}, the amount of signal generated per time step progressively decreases. The bystander molecules then produced and diffuse between neighboring voxels according to the diffusion Eq. (4):

$$\frac{d\rho}{dt}=-\theta\nabla^2\rho \tag{4}$$

where Θ is the diffusion coefficient, ρ is the signal concentration in the voxel, and ∇^2 denotes the Laplacian operator.

A fraction of the signal present at the previous time step decays over time, governed by the decay constant λ. This process continues until all cells have ceased signal production and the signal concentration in each voxel falls below a predefined threshold. At this point, the duration of exposure, during which each voxel experienced signal levels above the threshold, is calculated and translated into radiation-induced biological damage. Equation (5) describes the spatiotemporal evolution of signal concentration in each voxel by incorporating signal diffusion and decay.

$$\frac{\partial\rho\left(\vec{r},t\right)}{\partial t}=\theta\nabla^2\rho\left(\vec{r},t\right)-\lambda\rho\left(\vec{r},t\right) \tag{5}$$

However, for a complex system such as in vivo conditions, this equation can be modeled numerically. Numerical solutions enable the tracking of signal dynamics across space and time, albeit at the cost of increased

computational time. To numerically solve the above equation, the following approach is taken. First, the amount of signal produced at each time point, (ρ_{t,z_i}), is calculated using Eq. (2). The temporal evolution of the signal, resulting from diffusion and decay processes, is then described by the following Eq. (6):

$$\frac{\partial \rho}{\partial t} = \theta \frac{\partial^2 \rho}{\partial z^2} - \lambda \rho \tag{6}$$

For simplicity, the spatial variation of the signal in this equation is defined as one-dimensional, along the **z** direction only. However, this formulation can later be extended to a full three-dimensional distribution. In Eq. 6, if the volume containing the cells is discretized into a series of adjacent voxels z_i with width Δz, then based on the definition of the second derivative, we can express:

$$\left.\frac{\partial^2 \rho}{\partial z^2}\right|_{t,z_i} = \frac{\rho_{t,z_{i-1}} - 2\rho_{t,z_i} + \rho_{t,z_{i+1}}}{\Delta z^2} \tag{7}$$

By substituting Eq. (7) into Eq. (6), the following Equation was obtained:

$$\left.\frac{\partial \rho}{\partial t}\right|_{t,z_i} = \frac{\theta}{\Delta z^2}\left(\rho_{t,z_{i-1}} - 2\rho_{t,z_i} + \rho_{t,z_{i+1}}\right) - \lambda \rho_{t,z_i} \tag{8}$$

Then, the signal propagation pattern in the system can be predicted for each voxel at any given time:

$$\rho_{t+\Delta t,z_i} = \rho_{t,z_i} + \Delta t \left.\frac{\partial \rho}{\partial t}\right|_{t,z_i} \tag{9}$$

In these equations, Δt represents the time step used for simulating the system under study. As previously mentioned, this formulation is only valid under the assumption that the signal concentration varies due to diffusion in a single spatial direction. By discretizing the desired volume into a three-dimensional array of voxels, the signal distribution can be readily extended to three dimensions by incorporating the three-dimensional Laplacian equation:

$$\nabla^2 \rho = \frac{\partial^2 \rho}{\partial x^2} + \frac{\partial^2 \rho}{\partial y^2} + \frac{\partial^2 \rho}{\partial z^2} \tag{10}$$

Using the above equations, it is possible to calculate the signal level at any desired time for each specific voxel and determine the duration during which each voxel is exposed to a defined threshold level (ρ_t).

The greatest challenge in these calculations is that the diffusion rate has been very minimally characterized and quantified to date. Under in vivo conditions, it is not possible to accurately assess the diffusion behavior of signaling molecules. Therefore, certain assumptions must be made regarding this parameter. The effective range of bystander molecule movement (r) was converted to the diffusion coefficient (Θ) using the following equation:

$$r = \sqrt{\frac{\theta}{\lambda}} \tag{11}$$

This study considered a diffusion range of 10 mm (1 cm). Bystander signals have an effective range of 500 to 8000 micrometers[36–39]. Following McMahon et al., who originally proposed the bystander model employed here, we adopted a diffusion range of 10 mm to represent the upper plausible limit for passive signal spread in tissue. This value falls within a reasonable biological range and was deliberately chosen to amplify the observable impact of intercellular signaling on both tumor and normal tissues under spatially heterogeneous irradiation conditions. Longer-range propagation would likely require alternative transport mechanisms, which are beyond the scope of this model.

Increasing θ extends the reach of the bystander effect to more distant cells. The expression $\sqrt{\frac{\theta}{\lambda}}$ indicates exponential decay of signal strength as the distance from the irradiated voxel increases. The equation $\rho(\vec{r},t) = e^{-\sqrt{\frac{\theta}{\lambda}}\vec{r}}$ defines the boundary conditions for ρ, ensuring a gradual exponential signal decline at the simulation boundaries, assuming no external signaling sources.

The objective of our study is not to investigate the influence of parameter variations on the results. This study did not involve the purchase or direct use of these cell lines; instead, their parameters for computational modeling were obtained from published literature[15,20,33]. No direct experimentation was conducted on these cell lines. The fitted model parameters, including signal kinetics and cellular response metrics for each cell line, are presented in Table 1[15,20,33].

In this study, the AG01522 fibroblast cell line was used to represent normal tissue, while the H460 human non-small cell lung cancer (NSCLC) cell line represented tumor cells.

To simulate the proposed model on the treatment plans, patient CT scan slices and voxel-based dose information were extracted from the TPS. Using MATLAB code, all CT image slices were stacked to reconstruct the 3D volume, and the region of interest, along with its corresponding dose distribution, was obtained. Then, based on the derived dose matrix, signal production, diffusion, and decay were computed for each voxel. Using this information and another MATLAB-based program, the exposure time (τ) of each voxel to signals above a

H460	AG01522	Parameter
0.019 ± 0.002	0.019 ± 0.002	$\lambda(min^{-1})$
0.21 ± 0.02	0.21 ± 0.02	$\rho_{tthreshold}$
0.0029 ± 0.001	0.0027 ± 0.0007	$\kappa(min^{-1})$
132 ± 30	140 ± 10	$\gamma(min{\cdot}Gy^{-1})$
0.00008 ± 0.00003	0.00011 ± 0.00003	$\eta(min^{-1})$
1.9 ± 0.002	1.9 ± 0.002	Θ
0.78 ± 0.1	1.32 ± 0.017	HPG (hits/Gy)
3.7	1.2 ± 0.170	HB (hits)
1	1	ρ_{max}

Table 1. Input parameters of the bystander model for AG01522 and H460 cell lines[15,20,33].

certain concentration threshold was determined. The output of this process was a 3D matrix representing the duration each voxel was exposed to signal concentrations exceeding the threshold. Finally, this 3D matrix, along with a dose matrix of the same dimensions, was fed into another MATLAB script that calculated the survival fraction of each voxel based on the number of hits and a DNA damage model.

Intercellular signals in SFRT

To assess the impact of intercellular signaling, the survival fractions predicted by the bystander model were translated into biological dose (D_{bio}) equivalents. The biological dose is calculated by relating the observed survival probability for a voxel to a survival curve that characterizes the response of the same cell population under a perfectly uniform radiation field. Through this comparison, the biological dose can be derived using the interpolation technique. The biological dose distribution and the corresponding biological dose–volume histograms (D_{bio}VHs) offer a comprehensive characterization of how a cell population is affected by a given dose distribution, especially when radiation-induced intercellular signaling is taken into account. To facilitate comparison between different treatment plans, both the physical and biological doses were converted into equivalent uniform doses (EUDs). The EUD is the dose that, if delivered uniformly to the tumor volume, would result in the same average survival fraction as the given non-uniform irradiation. The EUD was determined by first simulating several uniform doses and calculating the survival probability for each dose level. Then, the average survival probability of the tumor volume was calculated. Using pre-calculated survival probabilities for the uniform doses, the dose that corresponded to this average survival probability was determined through interpolation. This value was taken as the EUD.

Valley-to-peak dose ratio (VPDR) calculation

The valley-to-peak dose ratio (VPDR) is a key dosimetric metric in SFRT, used to quantify dose heterogeneity within the gross tumor volume (GTV). It is commonly defined as the ratio of the mean dose (D_{mean}) received by 95–100% of the internal margin within the GTV to the prescribed peak dose Dp. Here, D_{mean}(95–100) represents the average dose received by the 5% of the internal margin exposed to the lowest doses, which can be obtained from the dose volume histogram (DVH) between 100 and 95% coverage[5,40].

Normal tissue complication probability (NTCP) calculation

The connection between partial irradiation of organs and resulting toxicity is a key concern for both radiobiologists and clinical oncologists. During radiotherapy, some exposure of healthy tissue to ionizing radiation is unavoidable, and normal tissue toxicity is often the primary constraint in effective treatment planning[15]. In this study, the Lyman–Kutcher–Burman (LKB) model was applied to compute normal tissue complication probability (NTCP) values for the surrounding three-dimensional normal tissues adjacent to the lung tumor, including the spinal cord, heart, and healthy lung tissue (Eqs. 12–15).

$$NTCP = \frac{1}{\sqrt{2\pi}} \int_{-\infty}^{t} e^{-\frac{t^2}{2}} dt \tag{12}$$

$$\upsilon = \frac{V}{V_{ref}} \tag{13}$$

$$t = \frac{(D - TD_{50}(\upsilon))}{(mTD_{50}(\upsilon))} \tag{14}$$

$$TD(\upsilon) = TD(1)\upsilon^{-n} \tag{15}$$

D represents the delivered dose, while V indicates the fraction of the organ volume exposed to radiation. TD stands for the organ's tolerance dose, and TD_{50} refers to the dose at which there is a 50% chance of complication. V_{ref} denotes the reference volume associated with TD_{50}. The parameter n characterizes how the complication probability varies with volume, and m defines the steepness of the dose–response curve. The LKB model, as described in Eqs. (12)–(15), operates under the assumption that part of the organ is uniformly irradiated

while the rest remains entirely unexposed, a simplification that does not accurately represent real clinical dose distributions[15]. The model can be modified to account for non-uniform dose distributions, using a method first introduced by Kutcher et al., to better reflect actual treatment scenarios[41]. The necessary equations for this modification are presented below.

$$(\delta Veff)_i = \delta V_i(\frac{D_i}{D_m})^{(\frac{1}{n})} \tag{16}$$

$$V_{eff} = \sum \left(\frac{D_i}{D_m}\right)^{\frac{1}{n}} \cdot \delta V_i \tag{17}$$

In this framework, the index *i* refers to a specific voxel within the target volume. D_i denotes the dose received by voxel *i*, and V_i corresponds to its volume contribution. The term $(\delta V_{eff})_i$ represents the adjusted effective volume, which is computed by assuming that the volume V_i, initially receiving dose D_i, instead receives the maximum dose D_m observed within the organ. Through the histogram reduction technique, a non-uniform dose distribution is transformed into an equivalent scenario where a portion of the effective organ volume V_{eff} uniformly absorbs D_m. At the same time, the remainder receives no dose, as described in Eqs. (15) and (16). This transformed data can then be used within the LKB model to estimate the normal tissue complication probability for the organ. To compute NTCP, the necessary inputs include organ-specific parameters n, m, and TD_{50}, as reported by Burman et al.[42].

In this study, the NTCP values were computed by considering both the physical and biological dose distributions of the treatment plans. Moreover, by imposing zero-flux boundary conditions on ρ at the organ boundaries, signal-mediated communication between adjacent organs was prevented.

Therapeutic ratio (TR) calculation

The therapeutic ratio (TR) is a quantitative indicator used to evaluate the normal tissue-sparing effectiveness of SFRT relative to a uniform dose distribution. In this study, we adopted the method proposed by Zwicker et al., which assumes a uniform distribution of normal cells within the tumor volume. This assumption is particularly relevant in clinical situations where the boundary between tumor and surrounding normal tissue is indistinct, and both cell populations may receive comparable radiation doses[17]. To calculate the TR, the EUD for the tumor was first computed, as previously described. Then, the mean survival fraction of normal cells within the SFRT field was estimated using the following equation:

$$\overline{\mathrm{SF}}_{\mathrm{Normal}}\,(\mathrm{SFRT}) = \frac{1}{N}\sum_{\mathrm{i}=0}^{\mathrm{N}} \mathrm{SF_i} \tag{18}$$

where SF_i represents the survival fraction in voxel i, derived from the bystander model. In the next step, the survival fraction of normal cells receiving a uniform dose equal to the EUD was estimated. Using a pre-calculated survival curve for normal cells under uniform irradiation, the survival fraction corresponding to the EUD was interpolated and denoted as SF_{normal} (EUD). The TR was then defined as:

$$\text{Therapeutic ratio} = \frac{\overline{\mathrm{SF}}_{\mathrm{normal}}\,(\mathrm{SFRT})}{\mathrm{SF}_{\mathrm{normal}}\,(\mathrm{EUD})} \tag{19}$$

A TR value greater than 1 implies that, for the same level of tumor control (achieved through the use of EUD), the SFRT plan results in greater preservation of normal cells compared to a uniformly delivered dose. This reflects a therapeutic advantage in favor of SFRT. A higher TR value thus reflects enhanced normal tissue sparing without compromising tumor control.

To evaluate the influence of intercellular signaling on TR, all calculations were performed under two conditions: (1) using only the physical dose distribution (i.e., with the diffusion range set to zero), and (2) incorporating signal propagation from high-dose regions to surrounding tissue. Differences in TR between these two scenarios were used to quantify the contribution of bystander effects to the overall TR.

Results

Figures 3 and 4 illustrate the physical dose distribution and the predicted changes due to intercellular signaling effects for the VMAT-GRID plan with prescribed doses of 15 and 20 Gy, respectively. Similarly, Figs. 5 and 6 present the corresponding results for the 3D-LRT plan with prescribed doses of 15 and 20 Gy, respectively.

These comparisons highlight variations in the tumor's dose distribution, emphasizing the impact of signaling effects on treatment outcomes. As observed, incorporating signaling effects into the dose distribution leads to significant deviation from the physical dose planning. The dose difference plots reveal increased cell killing, resulting in higher biological doses in low-dose regions due to signaling from adjacent higher-dose areas. Conversely, in high-dose regions, a slight reduction in biological doses is observed due to the more rapid decrease in signaling concentration near steep dose gradients.

As demonstrated by the VAMT-GRID and 3D-LRT plans in Figs. 3, 4, 5, 6, the inclusion of the bystander effect in dose planning leads to significant alterations in the distribution of cell death, thereby influencing the biological dose distribution. The most pronounced changes are observed in the 3D-LRT plan, where steep dose gradients cause substantial shifts in the biological dose (exceeding 0.92 Gy). In contrast, the VAMT-GRID plan

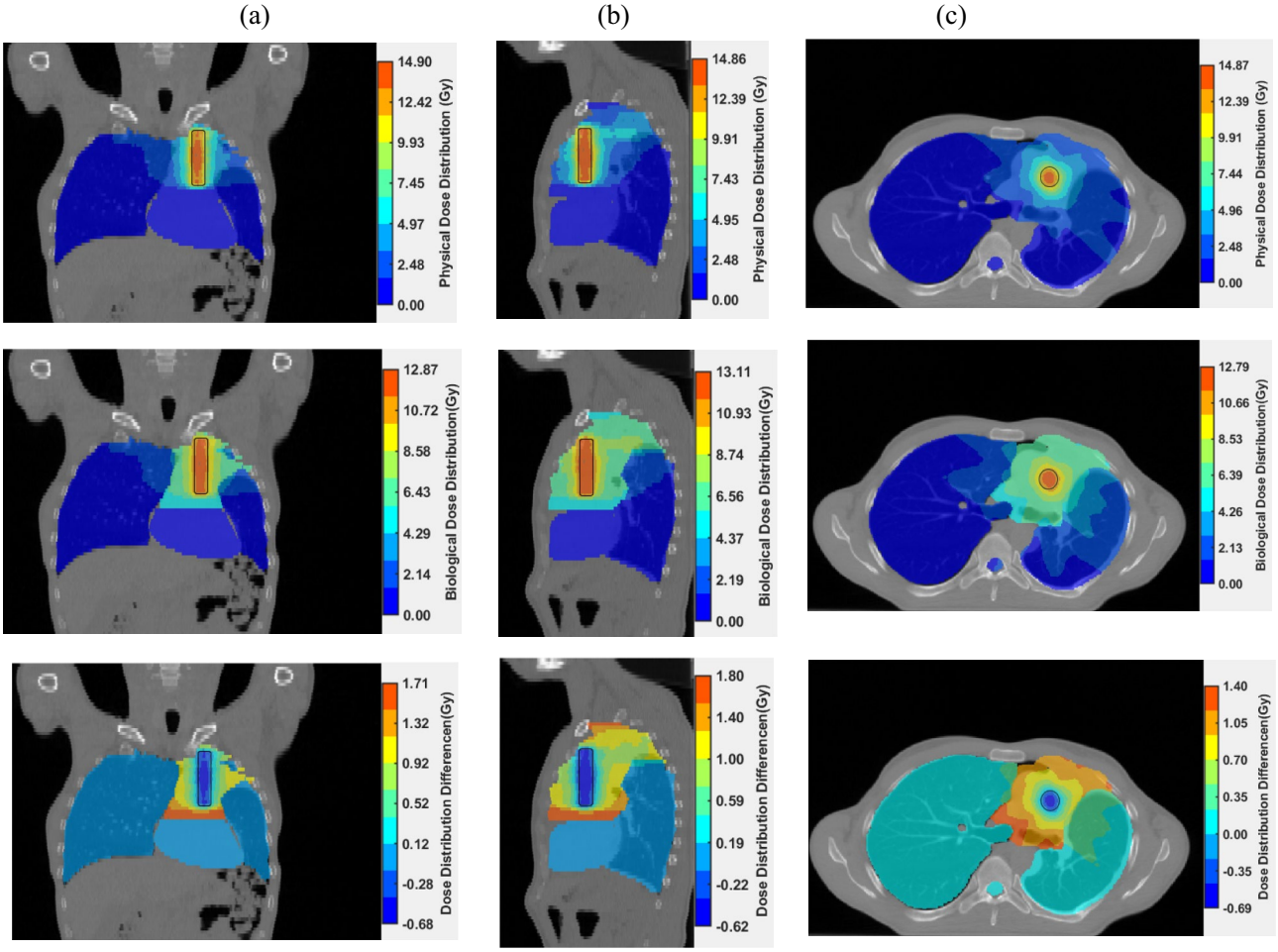

Fig. 3. Coronal (**a**), sagittal (**b**), and axial (**c**) views of the physical dose, biological dose, and dose differences for the VMAT-GRID plan with a 15 Gy dose. The first row presents the physical dose distribution as calculated by the TPS. The second row displays the biological dose distribution. The third row illustrates the differences between the physical and biological dose distributions. Negative values indicate a reduction, while positive values indicate an increase in the physical dose calculated by the TPS due to the inclusion of signaling effects.

shows relatively smaller changes in the dose distribution. It can be observed that these effects become more pronounced with increasing prescribed dose.

Table 2 shows that incorporating signaling effects leads to an increase in both the mean dose and the EUD of the GTV, with the 3D-LRT plan exhibiting a more pronounced increase than the VMAT-GRID plan. For a prescribed dose of 15 Gy, the mean dose and EUD increased by approximately 0.61 and 0.95 Gy in the 3D-LRT plan, respectively. The VMAT-GRID plan shows a smaller increase of 0.26 and 0.42 Gy. A similar result is obtained for the 20 Gy dose, where the mean dose and EUD increase by 1.14 and 0.85 Gy for the 3D-LRT plan and by 0.35 and 0.37 Gy in the VMAT-GRID plan.

Unlike the trends observed for the mean dose and EUD, intercellular signaling effects lead to a decrease in the TR, with a more significant reduction in the 3D-LRT plan compared to the VMAT-GRID plan. At a prescribed dose of 15 Gy, the TR decreases by 5.49 in the 3D-LRT plan, whereas the reduction in the VMAT-GRID plan is 3.05. Similarly, for a prescribed dose of 20 Gy, the TR drops by 4.84 in the 3D-LRT plan, while in the VMAT-GRID plan, the decrease is more modest, by 1.87.

To further quantify these effects, we calculated the relative percentage changes between the physical and biological values of key spatial dose metrics (Table 2). At a prescribed dose of 15 Gy, the biological EUD increased by approximately 5.0% for VMAT-GRID and 16.2% for 3D-LRT, compared to their physical counterparts. The corresponding increases in mean dose were 2.8 and 9.4%, respectively. The VPDR values showed modest increases of 3.6% for VMAT-GRID and 3.8% for 3D-LRT. Notably, the TR values decreased substantially due to the biological effect of intercellular signaling, with reductions of 38.1% for VMAT-GRID and 50.3% for 3D-LRT. Similarly, at a prescribed dose of 20 Gy, the biological EUD increased by 3.6% for VMAT-GRID and 13.8% for 3D-LRT. The mean dose rose by 3.0% and 15.3%, respectively. VPDR increased by 3.8% in VMAT-GRID and 10.5% in 3D-LRT. The TR values showed further reduction, decreasing by 23.1% for VMAT-GRID and 41.7% for 3D-LRT. These results demonstrate that while the differences in EUD, mean dose, and VPDR remain relatively modest, intercellular signaling has a more pronounced effect on TR, especially in 3D-LRT plans.

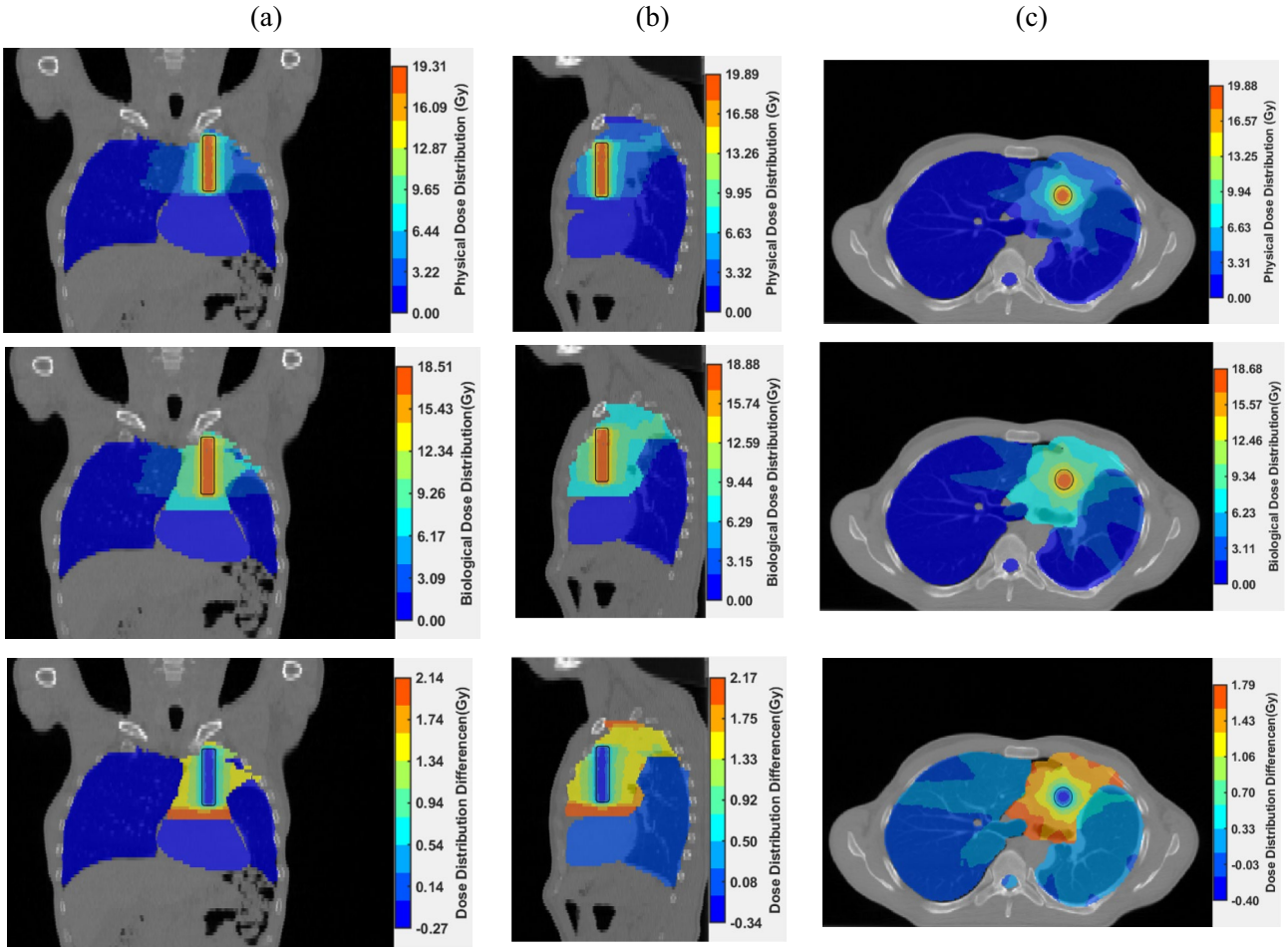

Fig. 4. Coronal (**a**), sagittal (**b**), and axial (**c**) views of the physical dose, biological dose, and dose differences for the VMAT-GRID plan with a 20 Gy dose. The first row presents the physical dose distribution as calculated by the TPS. The second row displays the biological dose distribution. The third row illustrates the differences between the physical and biological dose distributions. Negative values indicate a reduction, while positive values indicate an increase in the physical dose calculated by the TPS due to the inclusion of signaling effects.

Figures 7 and 8 illustrate the physical and biological DVHs of the GTV, grid target, and avoidance volumes for the VMAT-GRID and the 3D-LRT plans, respectively.

As expected, a noticeable difference is observed between the biological and physical DVHs for the GTV and avoidance volumes, particularly at lower doses. The cell killing induced by damaging signals from high-dose regions leads to a rightward shift in the biological DVHs. This effect becomes more pronounced at a prescribed dose of 20 Gy, especially in the 3D-LRT plan. In high-dose regions within the grid target volume, the opposite trend is observed, where the reduced contribution of signaling to cell death leads to a decrease in the biological dose.

Table 3 presents the NTCP values (expressed as percentages) for the right lung, left lung, heart, and spinal cord, calculated based on both physical and biological dose distributions at prescribed doses of 15 Gy and 20 Gy.

Across all evaluated scenarios, including two treatment techniques (VMAT-GRID and 3D-LRT) and two prescription dose levels (15 Gy and 20 Gy), the NTCP values for critical organs remain extremely low. In general, the biologically-based dose distributions yield slightly higher NTCP values than their physical counterparts; however, these differences are minimal. Increasing the dose from 15 to 20 Gy results in a slight rise in NTCP values for most organs in both plans and under both physical and biological dose distributions, indicating a relative increase in the probability of complications with dose escalation. However, these probabilities remain at low levels.

Discussion

Conventional radiation therapy planning typically assumes that cell death is determined solely by the absorbed dose at each location, without accounting for intercellular communication effects. While this approach is effective for uniform radiation fields, it may not provide accurate predictions for spatially modulated treatments such as SFRT, where intercellular signaling plays a significant role. These signaling effects can lead to outcomes that differ substantially from those predicted by traditional models[43]. In SFRT fields, despite highly non-uniform

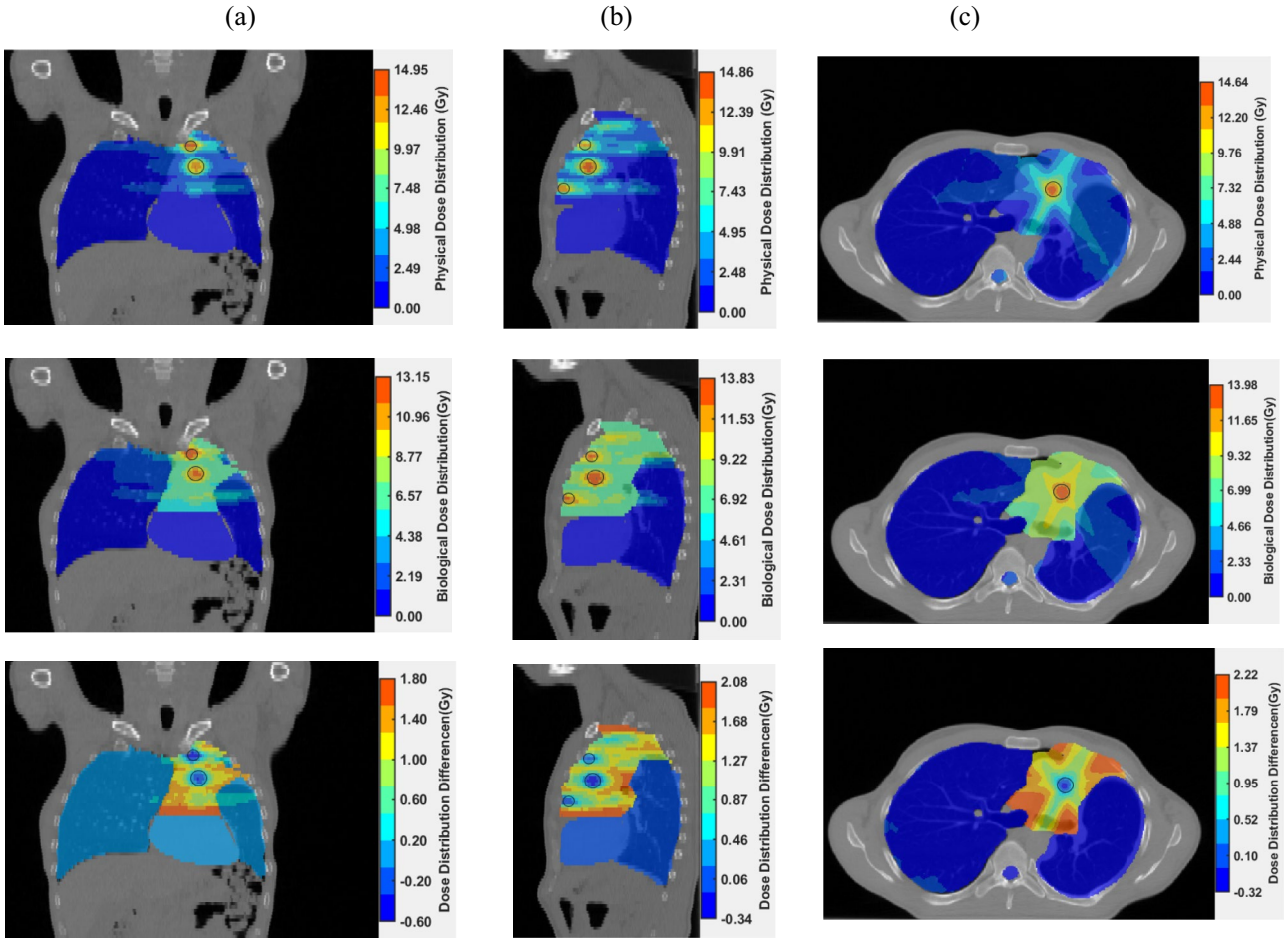

Fig. 5. Coronal (**a**), sagittal (**b**), and axial (**c**) views of the physical dose, biological dose, and dose differences for the 3D-LRT plan with a 15 Gy dose. The first row presents the physical dose distribution as calculated by the TPS. The second row displays the biological dose distribution. The third row illustrates the differences between the physical and biological dose distributions. Negative values indicate a reduction, while positive values indicate an increase in the physical dose calculated by the TPS due to the inclusion of signaling effects.

dose distributions with significantly low-dose regions, clinical observations consistently report uniform tumor regression. This suggests that signaling effects play a crucial role in treatment response[44,45]. However, these effects are not captured by the widely used linear-quadratic (LQ) model[23,24], raising concerns about its applicability to highly modulated dose treatments.

This study aimed to evaluate how the incorporation of intercellular signaling into modeling frameworks could influence key dosimetric and biological parameters relevant to the assessment of SFRT plans.

Figures 3, 4, 5, 6 demonstrate spatial deviations in biological dose distributions caused by intercellular signaling effects. These deviations are primarily localized within the GTV, especially in the 3D-LRT plan, where steep dose gradients and high peak doses amplify the biological response. In contrast, the surrounding normal tissues show negligible differences. Therefore, while the overall impact on NTCP values is minor, the local biological dose alterations within the tumor region may hold clinical significance and warrant further investigation.

The observed increase in cell killing within low-dose regions, alongside a reduction in biological dose in high-dose areas, reflects the complex interplay between intercellular signaling and physical dose gradients. These findings suggest that incorporating signaling effects into radiobiological modeling can uncover biologically meaningful dose redistributions that conventional models fail to capture.

Specifically, the biological dose distribution indicates that regions adjacent to high-dose zones benefit from enhanced cell killing due to intercellular signaling, resulting in a more spatially uniform biological response across the tumor. This phenomenon is supported by experimental studies showing that standard LQ models often underestimate cell death in spatially heterogeneous radiation fields. For instance, Peng et al.[24] demonstrated that including bystander effects in radiobiological models improves survival predictions by capturing additional cytotoxicity in low-dose regions not accounted for by the LQ model. Similarly, Butterworth et al.[23] reported that the LQ model tends to overestimate survival in shielded or low-dose areas, where signaling-mediated damage contributes significantly to biological response.

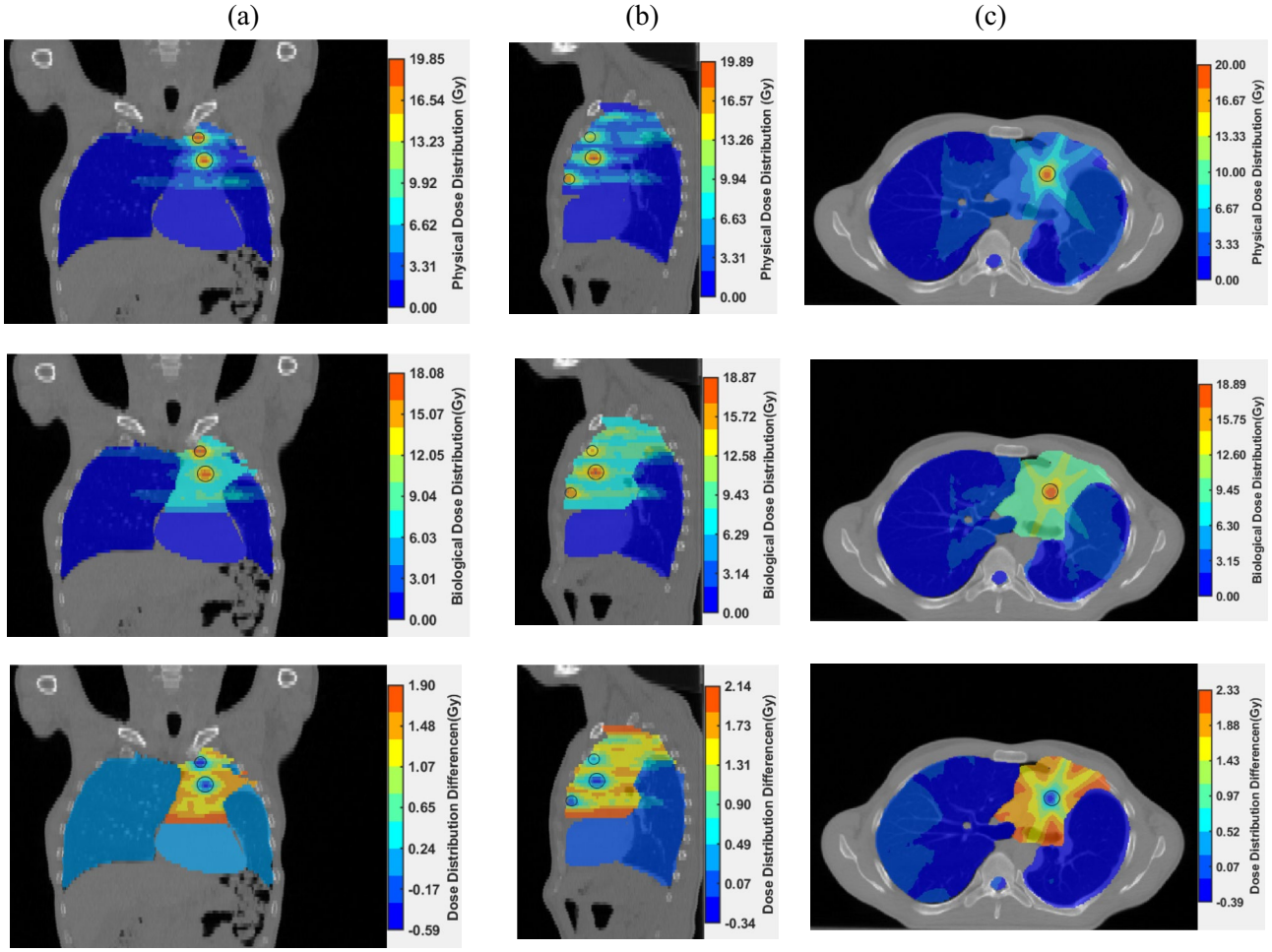

Fig. 6. Coronal (**a**), sagittal (**b**), and axial (**c**) views of the physical dose, biological dose, and dose differences for the 3D-LRT plan with a 20 Gy dose. The first row presents the physical dose distribution as calculated by the TPS. The second row displays the biological dose distribution. The third row illustrates the differences between the physical and biological dose distributions. Negative values indicate a reduction, while positive values indicate an increase in the physical dose calculated by the TPS due to the inclusion of signaling effects.

	A prescribed dose of 15 Gy				A prescribed dose of 20 Gy			
	VMAT-GRID		3D-LRT		VMAT-GRID		3D-LRT	
	Physical	Biological	Physical	Biological	Physical	Biological	Physical	Biological
EUD (Gy)	8.36	8.78	5.84	6.79	10.18	10.55	6.16	7.01
Mean dose (Gy)	9.39	9.65	6.5	7.11	11.52	11.87	7.44	8.58
VPDR (unitless)	0.28	0.29	0.26	0.27	0.26	0.27	0.19	0.21
TR (unitless)	8	4.95	10.9	5.41	8.1	6.23	11.6	6.76

Table 2. Impact of intercellular signaling on dosimetric parameters for GTV.

Notably, the divergence between LQ and signaling-based models becomes more pronounced in the presence of steep dose gradients, as demonstrated in prior simulations by Mahmoudi et al.[46]. These findings highlight the potential significance of intercellular signaling mechanisms in shaping biological dose distributions in spatially fractionated radiotherapy; however, further validation is needed to establish their relevance for clinical treatment planning.

Table 2 illustrates that signaling effects increase the mean dose, VPDR, and EUD while reducing the TR. The increase in VPDR can be attributed to the redistribution of biological dose, as bystander signals in high-dose regions diffuse toward adjacent low-dose areas. This leads to enhanced cell killing in valleys and a relative reduction in peak regions, smoothing the steep dose gradient and increasing the valley-to-peak dose ratio. Although the clinical significance of VPDR is not yet fully established, it is regarded as an important indicator of spatial heterogeneity in SFRT. Radiobiological hypotheses suggest that the lower VPDR values may enhance

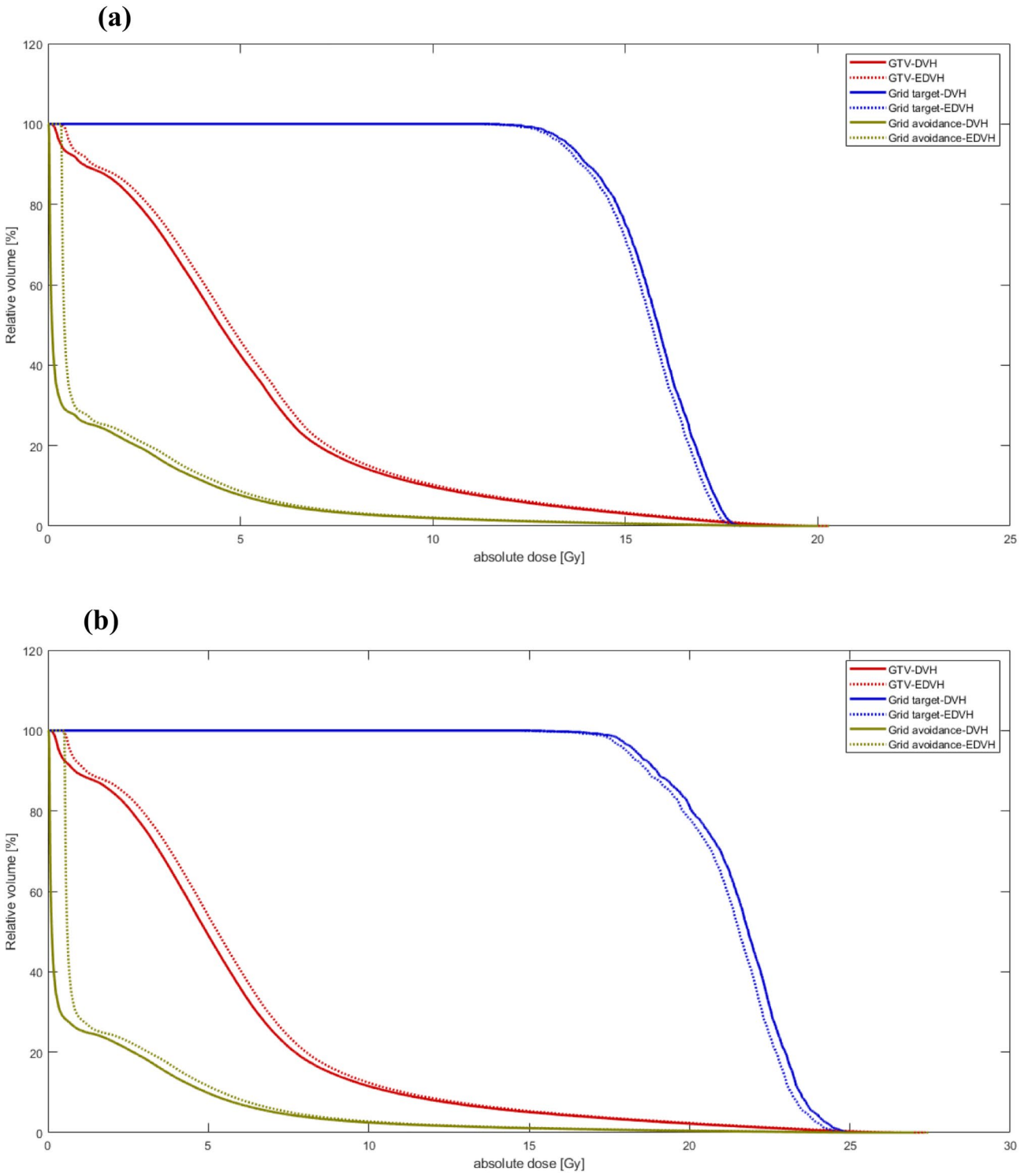

Fig. 7. Comparison of physical (solid line) and biological (dashed line) dose-volume histograms (DVHs) for the GTV, grid targets, and avoidance volumes in the VMAT-GRID plan, for prescribed doses of 15 Gy (**a**) and 20 Gy (**b**).

normal tissue sparing in valley regions. In addition, VPDR has been linked to immunologic mechanisms, as high-dose peaks may stimulate tumor antigen release and low-dose valleys may support the survival of immune cells involved in systemic anticancer responses[47,48]. Nevertheless, in our study, the differences in VPDR values with and without signaling effects remained relatively modest, suggesting that intercellular signaling may exert only a limited influence on this parameter under the modeled conditions.

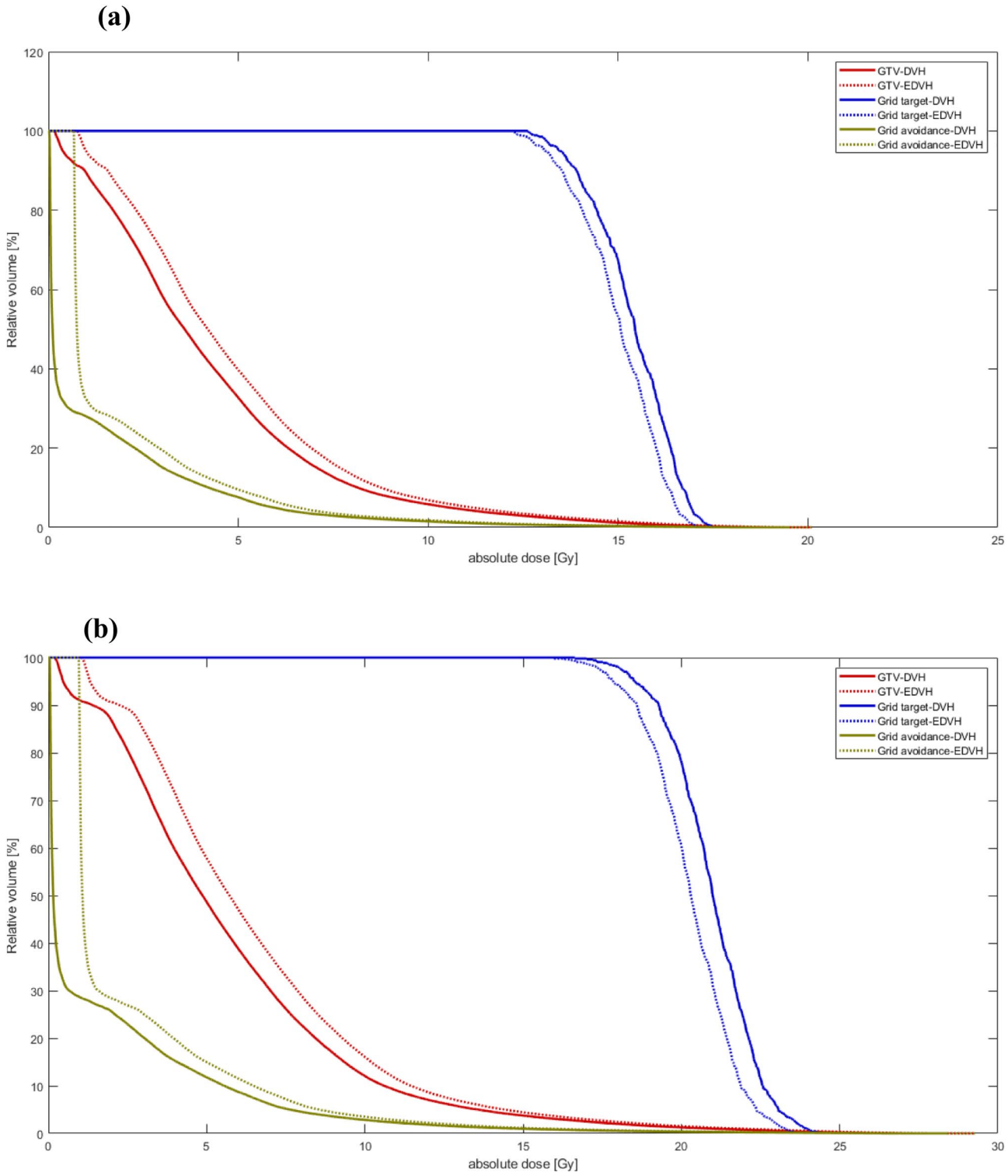

Fig. 8. Comparison of physical (solid line) and biological (dashed line) dose-volume histograms (DVHs) for the GTV, grid targets, and avoidance volumes in the 3D-LRT plan, for prescribed doses of 15 Gy (**a**) and 20 Gy (**b**).

The inclusion of signaling effects resulted in a moderate increase in EUD, reflecting the additional contribution of bystander-induced cell killing in low-dose regions. This increase suggests that the biological impact of the treatment is greater than what is predicted by the physical dose alone. Since the EUD is designed to represent a uniform dose that produces the same biological effect as the actual heterogeneous dose distribution, an increase in EUD indicates a greater potential for tumor control[7,48]. Although originally developed for

	A prescribed dose of 15 Gy				A prescribed dose of 20 Gy			
	VMAT-GRID		3D-LRT		VMAT-GRID		3D-LRT	
Organs	Physical	Biological	Physical	Biological	Physical	Biological	Physical	Biological
Right lung	0	0	0	5.40×10^{-17}	0	0	5.55×10^{-16}	5.67×10^{-16}
Heart	2.15×10^{-3}	2.20×10^{-3}	2.14×10^{-3}	2.20×10^{-3}	2.15×10^{-3}	2.22×10^{-3}	2.16×10^{-3}	2.25×10^{-3}
Left lung	3.40×10^{-3}	4.08×10^{-3}	3.26×10^{-3}	3.37×10^{-3}	3.84×10^{-3}	4.54×10^{-3}	4.85×10^{-3}	5.08×10^{-3}
Spinal cord	2.59×10^{-5}	2.67×10^{-5}	3.19×10^{-5}	3.31×10^{-5}	3.71×10^{-5}	3.95×10^{-5}	4.31×10^{-5}	4.45×10^{-5}

Table 3. NTCP Values (expressed as percentages) for physical and biological dose distributions.

conventional radiotherapy, EUD remains a widely used metric, and our findings suggest that its interpretation in SFRT contexts may be influenced by intercellular signaling.

The 3D-LRT plan shows more significant changes compared to the VMAT-GRID plan. For instance, the increase in mean dose and EUD in the 3D-LRT plan for both 15 and 20 Gy doses is nearly double that observed in the VMAT-GRID plan. This suggests that the 3D-LRT plan is more sensitive to signaling effects, likely due to its three-dimensional spatial dose modulation and steeper dose gradients. Three-dimensional spatial fractionation creates steep dose gradients, efficiently transmitting damaging signals from high-dose to low-dose regions in all directions, thereby increasing cellular damage in these areas. Therefore, in treatment plans with steeper dose gradients, such as 3D lattice therapy, careful consideration of intercellular signaling effects becomes increasingly important, as conventional LQ-based models may underestimate the biological impact in such highly modulated dose environments.

Including intercellular signaling effects leads to additional biological damage to non-irradiated cells in low-dose regions, particularly for normal tissues. While this also results in an increased EUD, potentially reducing normal tissue survival in the denominator of the TR calculation, the magnitude of this reduction is generally smaller than the signaling-induced decline in normal cell survival within the shielded regions of SFRT fields. Therefore, when signaling effects are incorporated into the model, the overall effect is a lower TR. This suggests that neglecting intercellular communication may lead to a misestimation of TR and an overly optimistic assessment of treatment safety. This highlights the importance of incorporating biological modeling into the analysis of spatially modulated dose distributions.

Figures 7 and 8 show that while the inclusion of signaling effects slightly reduces cell kill in the high-dose grid regions, it significantly increases cell kill in the low-dose subregions of the tumor. This effect is more pronounced in low-dose areas due to the additional cytotoxic impact of diffused bystander signals originating from high-dose zones. As a result, the signaling DVH of the GTV shifts rightward, suggesting a higher signaling dose and a more spatially uniform biological impact across the tumor. While this does not directly imply improved tumor control, it highlights the potential influence of intercellular signaling in modulating spatial dose effectiveness in SFRT. Moreover, comparison between Figs. 7 and 8 reveals that this effect is more pronounced in the 3D-LRT plan, particularly at higher prescription doses. This reflects the amplified impact of signaling due to dose fractionation in all three spatial dimensions. The presence of steeper dose gradients in 3D-LRT with higher prescribed dose facilitates more efficient diffusion and distribution of bystander signals, thereby enhancing the biological response in peripheral low-dose regions.

Based on the values presented in Table 3, it can be stated that considering bystander effects leads to an increase in NTCP values in all scenarios. This may be because the probability of complications for each organ is related to the total volume affected by radiation-induced toxicity, and accounting for intercellular signaling increases this effective volume. However, the signaling effects appear to be less pronounced in normal tissues, likely because the dose distribution in these regions is uniform[15]. The NTCP results obtained in this study are in agreement with the findings reported by Cahoon et al.[15], supporting the consistency of our model predictions with previously published data. Furthermore, a comparison of the results of this study with previous studies[15,49] highlights the benefit of delivering SFRT using VMAT, which distributes the dose over a large volume and reduces the exposure of critical organs.

As most previous studies have indicated, using conventional treatment regimens following the completion of SFRT is essential for achieving optimal tumor eradication. This is made possible by the enhanced protection of tissues outside the GTV provided by SFRT, which not only preserves the feasibility of additional treatment strategies but also allows patients receiving follow-up radiotherapy to achieve superior therapeutic outcomes[4,9,50,51].

The findings of this study align with previous research emphasizing the significance of bystander signaling in modulating tumor response to radiation[14,15,23,24]. In addition to bystander effects, other biological mechanisms may contribute to the complex response of tumors and normal tissues to SFRT. One such mechanism is radiation-induced immune modulation, which has been increasingly recognized as a relevant factor, particularly in the peritumoral regions receiving sublethal doses. Radiation can trigger immunogenic cell death, promote antigen presentation, and stimulate local and systemic immune responses, potentially enhancing tumor control. These immune-related effects, although not explicitly modeled in our study, may overlap with or even amplify bystander signaling pathways[1,3,7,11]. Future extensions of our modeling framework could incorporate immune dynamics to more comprehensively represent the multifaceted biological responses to SFRT.

Furthermore, the results are specific to the lung tumor model and VMAT-based SFRT plans used here; generalization to other tumor sites or spatial fractionation geometries (e.g., MBRT, MRT) remains uncertain.

Variations in high-dose region size, spacing, and the spatial scale of dose modulation may significantly alter intercellular signaling dynamics[19,46,52].

Given these uncertainties, before clinical implementation, rigorous biological validation, in vivo experimental studies, and parameter refinement are essential to ensure the reliability and generalizability of the proposed model.

Conclusion

This study highlights the pivotal role of bystander signaling in shaping both the dosimetric and biological outcomes of SFRT and reveals notable limitations of conventional models such as the LQ framework. The observed discrepancies between physical and biological dose metrics suggest that intercellular signaling may significantly influence treatment response, particularly in dose-escalated regimens and in scenarios with steep dose gradients, such as 3D-LRT. Notably, the findings indicate a relatively stronger impact of bystander effects in 3D-LRT compared to VMAT-GRID. However, these conclusions are hypothesis-generating rather than conclusive. Therefore, further experimental validation and refinement of biological parameters are essential steps toward enabling the clinical translation of these modeling insights.

Data availability

All relevant data are within the paper.

Received: 25 February 2025; Accepted: 14 July 2025
Published online: 05 August 2025

References

1. Prezado, Y. Divide and conquer: spatially fractionated radiation therapy. *Expert Rev. Mol. Med.* **24**, e3 (2022).
2. Mahmoudi, F., Shahbazi-Gahrouei, D. & Chegeni, N. The role of the spatially fractionated radiation therapy in the management of advanced bulky tumors. *Polish J. Med. Phys. Eng.* **27**, 123–135 (2021).
3. Prezado, Y. et al. Spatially fractionated radiation therapy: a critical review on current status of clinical and preclinical studies and knowledge gaps. *Phys. Med. Biol.* **69**, 10TR02 (2024).
4. Mohiuddin, M. et al. High-dose spatially-fractionated radiation (GRID): a new paradigm in the management of advanced cancers. *Int. J. Radiat. Oncol. Biol. Phys.* **45**, 721–727 (1999).
5. Wu, X. et al. The technical and clinical implementation of LATTICE radiation therapy (LRT). *Radiat. Res.* **194**, 737–746 (2020).
6. Slatkin, D. N., Spanne, P., Dilmanian, F. & Sandborg, M. Microbeam radiation therapy. *Med. Phys.* **19**, 1395–1400 (1992).
7. Zhang, H. & Mayr, N. A. *Spatially Fractionated, Microbeam and FLASH Radiation Therapy: A Physics and Multi-Disciplinary Approach* (IOP Publishing, 2023).
8. Billena, C. & Khan, A. J. A current review of spatial fractionation: Back to the future?. *Int. J. Radiat. Oncol. Biol. Phys.* **104**, 177–187 (2019).
9. Grams, M. P. et al. VMAT grid therapy: A widely applicable planning approach. *Pract. Radiat. Oncol.* **11**, e339–e347 (2021).
10. Joiner, M. C. & van der KogeJ, A. *Basic Clinical Radiobiology* (CRC Press, 2025).
11. Jenkins, S. V., Johnsrud, A. J., Dings, R. P. M. & Griffin, R. J. Bystander effects in spatially fractionated radiation therapy: From molecule to organism to clinical implications. *Semin. Radiat. Oncol.* **34**, 284–291 (2024).
12. Asur, R. S. et al. Spatially fractionated radiation induces cytotoxicity and changes in gene expression in bystander and radiation adjacent murine carcinoma cells. *Radiat. Res.* **177**, 751–765 (2012).
13. Mothersill, C., Rusin, A., Fernandez-Palomo, C. & Seymour, C. History of bystander effects research 1905-present; what is in a name?. *Int. J. Radiat. Biol.* **94**, 696–707 (2018).
14. Mahmoudi, F. et al. Potential implications of the radiation-induced bystander effect for spatially fractionated radiotherapy: A theoretical simulation study. *Int. J. Radiat. Res.* **20**, 657–664 (2022).
15. Cahoon, P. et al. Investigating spatial fractionation and radiation induced bystander effects: a mathematical modelling approach. *Phys. Med. Biol.* **66**, 225007 (2021).
16. Allen Li, X. et al. The use and QA of biologically related models for treatment planning: Short report of the TG-166 of the therapy physics committee of the AAPM. *Med. Phys.* **39**, 1386–1409 (2012).
17. Zwicker, R. D., Meigooni, A. & Mohiuddin, M. Therapeutic advantage of grid irradiation for large single fractions. *Int. J. Radiat. Oncol. Biol. Phys.* **58**, 1309–1315 (2004).
18. Niemierko, A. Reporting and analyzing dose distributions: a concept of equivalent uniform dose. *Med. Phys.* **24**, 103–110 (1997).
19. Gholami, S. et al. Is grid therapy useful for all tumors and every grid block design?. *J. Appl. Clin. Med. Phys.* **17**, 206–219 (2016).
20. McMahon, S. J. et al. A kinetic-based model of radiation-induced intercellular signalling. *PLoS ONE* **8**, e54526 (2013).
21. Ebert, M. A., Suchowerska, N., Jackson, M. A. & McKenzie, D. R. A mathematical framework for separating the direct and bystander components of cellular radiation response. *Acta Oncol.* **49**, 1334–1343 (2010).
22. Pakniyat, F. et al. Enhanced response of radioresistant carcinoma cell line to heterogeneous dose distribution of grid; the role of high-dose bystander effect. *Int. J. Radiat. Biol.* **96**, 1585–1596 (2020).
23. Butterworth, K. T. et al. Dose, dose-rate and field size effects on cell survival following exposure to non-uniform radiation fields. *Phys. Med. Biol.* **57**, 3197 (2012).
24. Peng, V. et al. Grid therapy using high definition multileaf collimators: realizing benefits of the bystander effect. *Acta Oncol.* **56**, 1048–1059 (2017).
25. Brenner, D. J., Little, J. & Sachs, R. The bystander effect in radiation oncogenesis: II. A quantitative model. *Radiat. Res.* **155**, 402–408 (2001).
26. Little, M. & Wakeford, R. The bystander effect in C3H 10T cells and radon-induced lung cancer. *Radiat. Res.* **156**, 695–699 (2001).
27. Nikjoo, H. & Khvostunov, I. K. Biophysical model of the radiation-induced bystander effect. *Int. J. Radiat. Biol.* **79**, 43–52 (2003).
28. Little, M., Filipe, J., Prise, K., Folkard, M. & Belyakov, O. A model for radiation-induced bystander effects, with allowance for spatial position and the effects of cell turnover. *J. Theor. Biol.* **232**, 329–338 (2005).
29. Stewart, R., Ratnayake, R. & Jennings, K. Microdosimetric model for the induction of cell killing through medium-borne signals. *Radiat. Res.* **165**, 460–469 (2006).
30. Shuryak, I., Sachs, R. K. & Brenner, D. J. Biophysical models of radiation bystander effects: 1. Spatial effects in three-dimensional tissues. *Radiat. Res.* **168**, 741–749 (2007).
31. Fakir, H., Hofmann, W., Tan, W. Y. & Sachs, R. K. Triggering-response model for radiation-induced bystander effects. *Radiat. Res.* **171**, 320–331 (2009).
32. Ryan, L. A., Smith, R. W., Seymour, C. B. & Mothersill, C. E. Dilution of irradiated cell conditioned medium and the bystander effect. *Radiat. Res.* **169**, 188–196 (2008).

33. McMahon, S. J. et al. A computational model of cellular response to modulated radiation fields. *Int. J. Radiat. Oncol. Biol. Phys.* **84**, 250–256 (2012).
34. Vines, A. M., Lyng, F. M., McClean, B., Seymour, C. & Mothersill, C. E. Bystander signal production and response are independent processes which are cell line dependent. *Int. J. Radiat. Biol.* **84**, 83–90 (2008).
35. Suchowerska, N., Ebert, M. A., Zhang, M. & Jackson, M. In vitro response of tumour cells to non-uniform irradiation. *Phys. Med. Biol.* **50**, 3041–3051 (2005).
36. Belyakov, O. V. et al. Biological effects in unirradiated human tissue induced by radiation damage up to 1 mm away. *Proc. Natl. Acad. Sci.* **102**, 14203–14208 (2005).
37. Gaillard, S., Pusset, D., De Toledo, S. M., Fromm, M. & Azzam, E. I. Propagation distance of the α-particle-induced bystander effect: the role of nuclear traversal and gap junction communication. *Radiat. Res.* **171**, 513–520 (2009).
38. Gaillard, S., Pusset, D., De Toledo, S., Azzam, E. & Fromm, M. Distance distribution of bystander effects in alpha-particle irradiated cell populations using a CR-39-based culture dish. *Radiat. Meas.* **43**, S34–S40 (2008).
39. Leonard, B. E. The range of the bystander effect signal in three-dimensional tissue and estimation of the range in human lung tissue at low radon levels. *Radiat. Res.* **171**, 374–378 (2009).
40. Zhang, X., Griffin, R. J., Galhardo, E. P. & Penagaricano, J. Feasibility study of 3D-VMAT-based GRID therapy. *Technol. Cancer Res. Treat.* **21**, 15330338221086420 (2022).
41. Kutcher, G., Burman, C., Brewster, L., Goitein, M. & Mohan, R. Histogram reduction method for calculating complication probabilities for three-dimensional treatment planning evaluations. *Int. J. Radiat. Oncol. Biol. Phys.* **21**, 137–146 (1991).
42. Burman, C., Kutcher, G., Emami, B. & Goitein, M. Fitting of normal tissue tolerance data to an analytic function. *Int. J. Radiat. Oncol. Biol. Phys.* **21**, 123–135 (1991).
43. Mahmoudi, F., Chegeni, N., Bagheri, A., Asl, J. F. & Batiar, M. T. Impact of radiobiological models on the calculation of the therapeutic parameters of Grid therapy for breast cancer. *Appl. Radiat. Isot.* **174**, 109776 (2021).
44. Huhn, J. L. et al. Spatially fractionated GRID radiation treatment of advanced neck disease associated with head and neck cancer. *Technol. Cancer Res. Treat.* **5**, 607–612 (2006).
45. Peñagarícano, J. A., Moros, E. G., Ratanatharathorn, V., Yan, Y. & Corry, P. Evaluation of spatially fractionated radiotherapy (GRID) and definitive chemoradiotherapy with curative intent for locally advanced squamous cell carcinoma of the head and neck: initial response rates and toxicity. *Int. J. Radiation Oncol. Biol. Phys.* **76**, 1369–1375 (2010).
46. Mahmoudi, F., Chegeni, N., Bagheri, A., Fatahi Asl, J. & Batiar, M. T. Impact of radiobiological models on the calculation of the therapeutic parameters of Grid therapy for breast cancer. *Appl. Radiat. Isot.* **174**, 109776 (2021).
47. Bräuer-Krisch, E. et al. Effects of pulsed, spatially fractionated, microscopic synchrotron X-ray beams on normal and tumoral brain tissue. *Mutat. Res.* **704**, 160–166 (2010).
48. Fontanella, A. N. et al. Effects of high-dose microbeam irradiation on tumor microvascular function and angiogenesis. *Radiat. Res.* **183**, 147–158 (2015).
49. Sheikh, K. et al. Comparison of treatment planning approaches for spatially fractionated irradiation of deep tumors. *J. Appl. Clin. Med. Phys.* **20**, 125–133 (2019).
50. Grams, M. P. et al. Clinical aspects of spatially fractionated radiation therapy treatments. *Phys. Med.* **111**, 102616 (2023).
51. Mohiuddin, M., Stevens, J. H., Reiff, J. E., Huq, M. S. & Suntharalingam, N. Spatially fractionated (GRID) radiation for palliative treatment of advanced cancer. *Radiat. Oncol. Investig. Clin. Basic Res.* **4**, 41–47 (1996).
52. Gholami, S. et al. Grid block design based on Monte Carlo simulated dosimetry, the linear quadratic and Hug-Kellerer radiobiological models. *J. Med. Phys.* **42**, 213–221 (2017).

Author contributions

E. Balvasi performed treatment planning, and programming, analyzed the data, and wrote the manuscript. F. Mahmoudi contributed to the concept and design of the treatment plans and supervised the data analysis. P. Farnia selected the CT scan images of patients' lungs suitable for SFRT and programming. F. Jafari performed image contouring and evaluated the treatment plans. Gh. Geraily supervised the treatment planning process and gave final approval for the manuscript. All authors reviewed and approved the final manuscript.

Declarations

Competing interests

The authors declare no competing interests.

Ethical declarations

The ethical declaration was obtained from the Ethics Committee of Tehran University of Medical Sciences (Ethics code: IR.TUMS.IKHC.REC.1402.160).

Additional information

Correspondence and requests for materials should be addressed to F.M. or G.G.

Reprints and permissions information is available at www.nature.com/reprints.

Publisher's note Springer Nature remains neutral with regard to jurisdictional claims in published maps and institutional affiliations.